J. Fluid Mech. (2007), *vol.* 577, *pp.* 53–77. © 2007 Cambridge University Press
doi:10.1017/S002211200600437X Printed in the United Kingdom

Lock-exchange flows in sloping channels

V. K. BIRMAN[1], B. A. BATTANDIER[1,2], E. MEIBURG†[1] AND P. F. LINDEN[3]

[1]Department of Mechanical Engineering, University of California, Santa Barbara, CA 93106, USA
[2]Ecole Polytechnique, 91128 Palaiseau Cedex, France
[3]Department of Mechanical and Aerospace Engineering, University of California, San Diego, CA 92093, USA

(Received 10 March 2006 and in revised form 17 October 2006)

Two-dimensional variable-density Navier–Stokes simulations have been conducted in order to investigate the effects of a slope on the classical lock-exchange flow. Simulations of full lock releases show that the flow goes through an initial quasi-steady phase that is characterized by a constant front velocity. This quasi-steady front velocity has a maximum for slope angles around 40°, and it persists up to a dimensionless time of the order of 10. The flow subsequently undergoes a transition to a second phase with a larger, unsteady, front velocity. These computational findings were confirmed by experimental observations of lock-exchange flows in a tube of circular cross-section.

The reason for the observed transition from a quasi-steady front velocity to a larger, unsteady, value is found in the continuous acceleration of the stratified fluid layers connecting the two fronts by the streamwise component of the gravity vector. This acceleration leads to a situation where the fluid layers behind the current front move faster than the front itself. Initially the resulting addition of fluid to the current front from behind affects only the size of the front, while its velocity remains unchanged. Eventually, the current front is unable to absorb more fluid from behind and its velocity has to increase, thereby triggering the transition to the second, unsteady, phase. The transition time is determined as a function of the slope and the density ratio of the two fluids. For increasing density contrast, the transition is seen to occur earlier for the denser current.

Conceptually simple models based on the analysis by Thorpe (1968) are compared with simulation results for the flow in the region connecting the fronts. For the early stages of the flow a two-layer stratification model is found to be appropriate, while the later stages require a three-layer stratification model, owing to the intense mixing in the central part of the channel cross-section. These models are employed to estimate the time after which the accelerating stratified fluid layers will affect the velocities of the current fronts. They provide upper and lower estimates for the transition time which are in good agreement with the simulation results.

1. Introduction

Gravity currents, sometimes also called density or buoyancy currents, form as a result of predominantly horizontal density gradients in fluids. They play a central role in a variety of geophysical situations and industrial applications, as described in

† Author to whom correspondence should be addressed.

https://doi.org/10.1017/S002211200600437X Published online by Cambridge University Press

the comprehensive introduction to this topic by Simpson (1997). The lock-exchange set-up has long served as a paradigm configuration for studying the spatio-temporal evolution of gravity currents. Among the first authors to address this geometry, Huppert & Simpson (1980) demonstrated the existence of three distinct phases in lock-exchange flows over horizontal surfaces; see also the related experimental investigations of Britter & Simpson (1978) and Simpson & Britter (1979). The initial phase is characterized by a gravity current propagating with a constant front velocity. Once the disturbance generated by the endwall overtakes the front, the slumping phase gives way to a self-similar inertial phase during which the front slows down (Rottman & Simpson 1983). Eventually a phase is reached in which the buoyancy forces are balanced by viscous forces. For full-depth lock releases the initial constant-front velocity is generally well captured by the classical energy-conserving theory of Benjamin (1968). For a critical discussion of Benjamin's analysis, along with an alternative theory, the reader is referred to the recent work of Shin, Dalziel & Linden (2004). A central question of the present study is how the above well-established succession of distinctly different phases is modified by the presence of a sloping bottom.

This initial series of lock-exchange investigations was subsequently extended in several different directions. Hallworth *et al.* (1993) developed a new pH-based method to study entrainment in turbidity currents. They showed by dimensional analysis that the entrainment of ambient fluid in gravity currents depends only on the initial lock volume and the distance from the release location. The work was extended further to two-dimensional and axisymmetric turbulent gravity currents in Hallworth *et al.* (1996). Hacker, Linden & Dalziel (1995) studied the effect of the lock's aspect ratio on the entrainment rate for gravity currents on a horizontal surface. They also discussed the development of different internal structures due to differences in the entrainment rate. The direct numerical simulations of Härtel, Meiburg & Necker (2000) and Cantero *et al.* (2006) provide highly resolved information on mixing and dissipation. The lock-exchange experiments Gröbelbauer, Fanneløp & Britter (1993) focus on non-Boussinesq effects, as do the more recent theoretical (Lowe, Rottman & Linden 2005) and numerical (Birman, Martin & Meiburg 2005; Etienne, Hopfinger & Saramito 2005) modelling efforts. In these studies, strong density differences are seen to result in distinctly different front heights, propagation velocities and overall dynamics for the light and the heavy fronts.

When the driving force is provided by particle loading rather than compositional variations, a host of new phenomena arise, as discussed in the investigations by Bonnecaze, Huppert & Lister (1993), Bonnecaze & Lister (1999) and Necker *et al.* (2002, 2005). Such particle-driven flows frequently occur over sloping bottoms, e.g. in the form of powder snow or pyroclastic avalanches or as sediment-driven turbidity currents that propagate from the continental shelf down the continental slope to the deep ocean. These examples differ from lock-exchange situations in that they are not confined by side or top walls, so that the flow domain is essentially infinite. The propagation of a given volume of heavy fluid down a slope should thus proceed in a self-similar fashion, a fact that was confirmed by the investigation of Beghin, Hopfinger & Britter (1981). By coupling scaling laws for the balance of inertial and buoyancy forces with mass-conservation arguments that include the effects of entrainment, these authors were able to derive a closed-form similarity solution. The theory predicts the velocity of the centre of mass to increase initially and to decrease during the later stages of the flow. The theoretical solutions for both these phases are in good agreement with corresponding experimental observations. This problem has been revisited recently by Maxworthy & Nokes (2006), who found that for larger

https://doi.org/10.1017/S002211200600437X Published online by Cambridge University Press

buoyancy releases the dynamics become more complicated, owing to the interaction of the current front with the trailing sections of the fluid. These authors employed dimensional analysis in order to arrive at a more refined description of the flow. Webber, Jones & Martin (1993) and Tickle (1996) presented similarity solutions to the shallow-water equations and proposed wedge models for three-dimensional gravity-current releases on slopes. Ross, Linden & Dalziel (2002) performed corresponding experiments and extended the wedge models to include the effects of entrainment.

Some applications of gravity currents down inclined slopes are appropriately described by the lock-exchange geometry, such as the propagation of accidentally released methane in a mine, the ventilation of vehicular tunnels and the spreading of hot products resulting from a tunnel fire. Earlier investigations of gravity currents in sloping channels include that by Ellison & Turner (1959), who measured the entrainment as a function of the Richardson number. Britter & Linden (1980) focused on the head of a gravity current in an inclined deep channel. Importantly, they investigated the situation produced by a continuous supply of dense fluid, which is different in some aspects from the full-depth finite-release lock-exchange flow studied here. Britter & Linden (1980) reported that the current front propagates at an approximately constant velocity for all but very small angles. The authors furthermore noted that the head size increases not only by entrainment from the ambient but also as a result of flow into the head from the trailing portions of the current.

In lock-exchange flows, a region of stably stratified shear flow forms throughout the central section of the channel, where the lighter fluid is situated above the heavier. In a horizontal channel, this flow is driven by 'end effects' only, i.e. by the conditions outside the central section. For a sloping bottom, however, gravity continues to be a driving force throughout the entire stratified-flow region. This situation was investigated by Thorpe (1968, 1971), although in his experiments it was approached from a set of initial conditions that, in some sense, were diametrically opposed to the lock-exchange configuration. The initial set-up in Thorpe (1968) consisted of a horizontal channel with closed ends containing a stably stratified fluid at rest. After the channel was tilted, a continuously accelerated stratified shear flow evolved in the central section of the channel that persisted until it was modified by surges propagating from the endwalls. The author presented a unidirectional flow model for the stratified shear flow which was in good agreement with the experimental observations until the onset of a shear-driven Kelvin–Helmholtz instability, which was further studied theoretically in Thorpe (1971). Parts of the flow model developed by Thorpe (1968) will be employed in the present investigation.

The paper is structured as follows. Section 2 describes the physical problem and the set-up for the simulations, along with the governing equations and the boundary and initial conditions. The computational approach is briefly outlined in § 3. Section 4 presents the simulation results. Both the height and velocity of the front will be analysed, along with the ensuing mixing, as functions of the slope angle and the density ratio. Experimental data for the front velocity will be presented in § 5. The simple model of Thorpe will be adapted, in § 6, to explain certain aspects of the simulation results. A brief summary section concludes the paper.

2. Problem formulation

The investigation focuses on a rectangular channel of height H and length L (figure 1) which is filled with two miscible fluids that are initially separated by a membrane located at a distance L_1 from the left-hand wall. The x-axis is parallel to

https://doi.org/10.1017/S002211200600437X Published online by Cambridge University Press

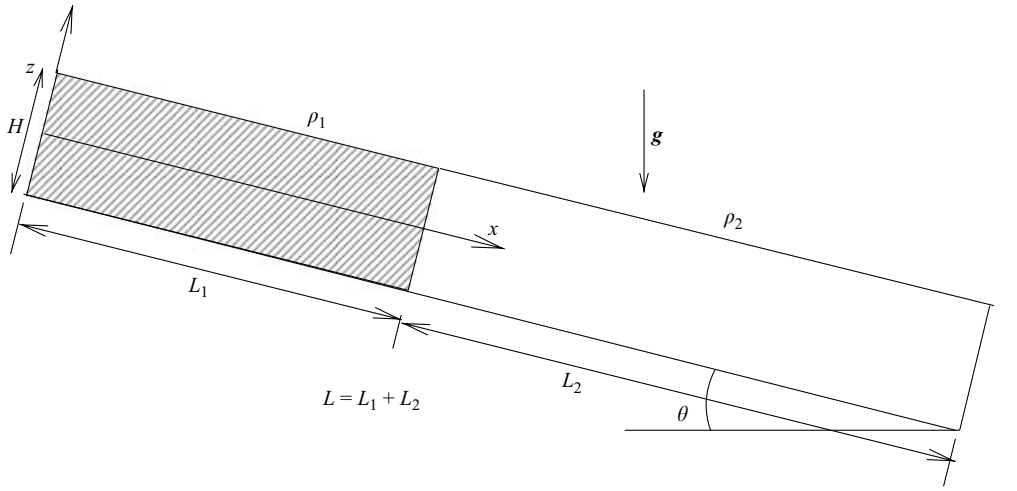


FIGURE 1. The lock-exchange configuration in a sloping channel. A membrane initially divides the rectangular container of length L and height H into two compartments of length L_1 and $L_2 = L - L_1$. The left-hand chamber is filled with fluid of density ρ_1, while the right-hand chamber contains fluid of density ρ_2. The container is tilted at an angle θ with respect to the horizontal. Upon removal of the membrane, a dense front moves rightwards along the lower boundary, while a light front propagates leftwards along the upper boundary.

the sloping bottom, while the left- and right-hand endwalls point in the z-direction. The fluid in the left-hand compartment has density ρ_1, and the right-hand reservoir holds a fluid of density $\rho_2 < \rho_1$. This initial configuration causes a discontinuity of the hydrostatic pressure across the membrane, which sets up a flow predominantly in the x-direction once the membrane is removed. The denser fluid moves rightwards along the bottom of the channel, while the lighter fluid moves leftwards along its top.

For the analysis of the resulting flow, we employ the incompressible variable-density Navier–Stokes equations without invoking the Boussinesq approximation; see Birman, Martin & Meiburg (2005). The buoyancy velocity

$$u_b = \sqrt{g'H} \quad \text{with} \quad g' = g\frac{\rho_1 - \rho_2}{\rho_1} \tag{2.1}$$

is taken as the characteristic velocity and H as the representative length scale; the larger density ρ_1 serves as the characteristic density. Alternatively, $u_b = \sqrt{g'H}/\cos\theta$ can be employed as the characteristic velocity; see Séon, Hulin & Salin (2005). This scaling can be useful for capturing the effects of relatively small angles when the current travels faster. However, it results in unreasonably large characteristic velocities for larger values of θ and in $u_b \to \infty$ for $\theta \to 90°$. Since the present investigation will not be limited to small angles, we employ the characteristic velocity ρ_1, which does not depend on the angle. In dimensionless form the governing equations thus read

$$\frac{1}{\rho}\frac{\mathrm{D}\rho}{\mathrm{D}t} + \nabla\cdot\boldsymbol{u} = 0, \tag{2.2}$$

$$\rho\frac{\mathrm{D}\boldsymbol{u}}{\mathrm{D}t} = \frac{1}{1-\gamma}\rho\boldsymbol{e}_g - \nabla p + \frac{1}{Re}\nabla\cdot(2\rho\boldsymbol{S}), \tag{2.3}$$

$$\frac{\mathrm{D}\rho}{\mathrm{D}t} = \frac{1}{Pe}\nabla^2\rho. \tag{2.4}$$

https://doi.org/10.1017/S002211200600437X Published online by Cambridge University Press

Here $\mathrm{D}/\mathrm{D}t$ denotes the material derivative of a quantity, $\boldsymbol{u}=(u, w)^T$ indicates the velocity vector and p the pressure; $\boldsymbol{e}^g=(\sin\theta, -\cos\theta)$ represents the unit vector pointing in the direction of gravity, $\gamma=\rho_2/\rho_1$ is the density ratio, $\boldsymbol{S}$ denotes the rate-of-strain tensor and θ is the angle of inclination of the channel bottom with respect to the horizontal direction; see figure 1.

It is instructive to conduct an order-of-magnitude analysis of the terms in the continuity equation (2.2); see also the discussion in Joseph & Renardy (1992). Equation (2.4) suggests that, in dimensional quantities,

$$\frac{\mathrm{D}\rho}{\mathrm{D}t} \sim \kappa \frac{\partial^2 \rho}{\partial x^2} \sim \kappa \frac{\rho}{\delta^2}, \tag{2.5}$$

where δ is the thickness of the layer over which the density varies. This thickness is determined by the balance of strain and diffusion:

$$\rho \frac{\partial u}{\partial x} \sim \kappa \frac{\partial^2 \rho}{\partial x^2}. \tag{2.6}$$

With $\partial u/\partial x \sim u_b/H$, this yields

$$\delta \sim \sqrt{\frac{\kappa H}{u_b}}. \tag{2.7}$$

Hence, in the continuity equation (2.2), $(1/\rho)\mathrm{D}\rho/\mathrm{D}t$ is formally of the same order as $\partial u/\partial x$. However, the term $(1/\rho)\mathrm{D}\rho/\mathrm{D}t$ is confined to the thin concentration boundary layers, of thickness δ; it approaches zero everywhere else. Furthermore, since $\partial^2\rho/\partial x^2$ changes sign across the concentration layer, it involves a positive and a negative contribution within the layer. For thin-concentration boundary layers, these contributions cancel each other approximately, resulting in an even smaller far-field effect. Since δ scales as

$$\frac{\delta}{H} \sim Pe^{-1/2}, \tag{2.8}$$

the region over which the term $(1/\rho)\mathrm{D}\rho/\mathrm{D}t$ is non-zero decreases as Pe increases. Clearly, in the limit $Pe \to \infty$, i.e. in the absence of diffusion, the substantial derivative vanishes everywhere. The above argument shows that for high-Pe flows, everywhere outside-narrow the concentration boundary layers, the velocity-derivative terms balance each other in the continuity equation while the material-derivative term enters into this balance only within the concentration boundary layers. Hence, omitting the material-derivative term in the continuity equation is justified for high-Pe flows, on which our current interest focuses. Consequently, we employ the simplified set of dimensionless equations

$$\nabla \cdot \boldsymbol{u} = 0, \tag{2.9}$$

$$\rho \frac{\mathrm{D}\boldsymbol{u}}{\mathrm{D}t} = \frac{1}{1-\gamma}\rho \boldsymbol{e}_g - \nabla p + \frac{1}{Re}\nabla \cdot (2\rho \boldsymbol{S}), \tag{2.10}$$

$$\frac{\mathrm{D}\rho}{\mathrm{D}t} = \frac{1}{Pe}\nabla^2 \rho. \tag{2.11}$$

In further support of this approach, we note that in all our simulations the initial mass of the denser fluid was conserved to within one half of one per cent, even over long times. Finally, earlier simulations based on the same formulation (Birman *et al.* 2005) and corresponding experimental data showed excellent agreement.

The fluids are assumed to have identical kinematic viscosities ν. Besides γ, the Reynolds number Re and the Péclet number Pe appear in the above equations; they

https://doi.org/10.1017/S002211200600437X Published online by Cambridge University Press

are defined as

$$Re = \frac{u_b H}{\nu}, \quad Pe = \frac{u_b H}{\kappa}, \tag{2.12}$$

where κ represents the constant diffusion coefficient of the two fluids. They are related by the Schmidt number

$$Sc = \frac{\nu}{\kappa}, \tag{2.13}$$

which represents the ratio of kinematic viscosity and molecular diffusivity. Test calculations showed the effect of variations in Sc to be very small, so that we took $Sc = 1$ for all cases; see also Necker *et al.* (2005). A detailed discussion of the above governing equations is given in Birman *et al.* (2005) and will not be repeated here.

For the purpose of performing two-dimensional numerical simulations, we recast the above equations (2.9) and (2.10) into the streamfunction–vorticity (ψ, ω) formulation. With

$$\omega = \frac{\partial w}{\partial x} - \frac{\partial u}{\partial z}, \tag{2.14}$$

$$u = \frac{\partial \psi}{\partial z}, \tag{2.15}$$

$$w = -\frac{\partial \psi}{\partial x}, \tag{2.16}$$

we obtain

$$\nabla^2 \psi = -\omega, \tag{2.17}$$

$$\frac{\mathrm{D}\omega}{\mathrm{D}t} = \frac{1}{Re}\nabla^2 \omega - \frac{\rho_x}{(1-\gamma)\rho}\cos\theta - \frac{\rho_z}{(1-\gamma)\rho}\sin\theta + \frac{\rho_z}{\rho}\frac{\mathrm{D}u}{\mathrm{D}t} - \frac{\rho_x}{\rho}\frac{\mathrm{D}w}{\mathrm{D}t} + \frac{1}{\rho Re}\{2\rho_x \nabla^2 w - 2\rho_z \nabla^2 u + 4\rho_{xz} w_z + (u_z + w_x)(\rho_{xx} - \rho_{zz})\}. \tag{2.18}$$

We have $\psi = 0$ along all boundaries. We will investigate both slip and no-slip boundary conditions along all walls, resulting in corresponding boundary conditions for the vorticity field. The normal derivative of the concentration vanishes along all walls, thus enforcing zero diffusive mass flux.

3. Computational approach

The simulations employ equidistant grids in a rectangular computational domain. A Fourier spectral approach is used for the streamfunction and vorticity variables in the streamwise x-direction:

$$\psi(x, z, t) = \sum_l \hat{\psi}_l(z, t)\sin(l\alpha x), \tag{3.1}$$

$$\omega(x, z, t) = \sum_l \hat{\omega}_l(z, t)\sin(l\alpha x), \tag{3.2}$$

where

$$|l| < \frac{N_1}{2}, \quad \alpha = \frac{2\pi}{L}. \tag{3.3}$$

Here N_1 denotes the number of grid points in the x-direction. The z-derivatives are approximated by compact finite differences; see Lele (1992). As in the Boussinesq

https://doi.org/10.1017/S002211200600437X Published online by Cambridge University Press

investigation of Härtel, Meiburg & Necker (2000), the density derivatives are computed by means of compact finite differences in both directions. At interior points, sixth-order spatially accurate stencils are used, with third- and fourth-order accurate stencils employed at the boundaries. The flow field is advanced in time by means of a third-order Runge–Kutta scheme, as described by Härtel *et al.* (2000). The material derivatives of the velocity components appearing in the vorticity equation (2.18) are computed by first rewriting them in terms of the local time derivative plus the convective terms. The spatial derivatives appearing in the convective terms are then evaluated in the usual high-order way. The local time derivative is computed by backward extrapolation as follows:

$$\left[\frac{\partial \boldsymbol{u}}{\partial t}\right]^n = \frac{\boldsymbol{u}^n - \boldsymbol{u}^{n-1}}{\Delta t}. \tag{3.4}$$

This approach was shown by Birman *et al.* (2005) to work well. The Poisson equation for the streamfunction (2.17) is solved by compact finite differences once per time step in Fourier space, according to

$$\left(\hat{\psi}_l^{m+1}\right)'' - (l\alpha)^2 \hat{\psi}_l^{m+1} = -\hat{\omega}_l^{m+1}, \tag{3.5}$$

the prime denoting differentiation with respect to z. We typically employed $L = 28$ and $L_1 = 10$ in the simulations, with 2049×250 grid points.

4. Simulation results

While the present investigation focuses on the lock-exchange configuration, deep-water finite-volume releases on sloping bottoms have also been addressed in the past; see Beghin *et al.* (1981). These authors conducted experiments and derived a similarity solution based on mass-conservation arguments coupled with a balance of inertial and gravitational forces. As a preliminary step, and for validation purposes, we performed corresponding numerical simulations, which demonstrated good agreement with the experimental data.

4.1. *Representative Boussinesq case*

We begin by describing results from a representative case with a slope of 30° and a density ratio $\gamma = 0.998$, at which the Boussinesq approximation is valid. Figure 2 shows contour plots of the concentration fields for $Re = 4000$, a channel length $L = 28$ and a lock length $L_1 = 10$. The channel was divided unevenly so that we could run the longest possible simulation before the dense current reached the endwall without being overtaken by the reflected bore. The flow in the sloping channel may be compared with its horizontal counterpart at various times. During the initial phase the effect of the slope is seen to be minimal, as the concentration contours for the horizontal and the sloping channels are very similar.

With increasing time, more substantial differences between the two flows emerge. At $t = 6$ the flow in the horizontal channel is characterized by an interfacial region that exhibits moderate-sized vortices aligned predominantly in the horizontal direction, figure 2(*d*). The sloping-channel case, however, exhibits a large-scale turnover event that nearly extends to the top and bottom walls, figure 2(*c*), and results in more mixing across the height of the channel. This enhanced mixing behaviour of the flow in the sloping channel is maintained until the end of the simulation, at $t = 12$. The fronts progress farther in the sloping channel than in the horizontal channel, reflecting an

https://doi.org/10.1017/S002211200600437X Published online by Cambridge University Press

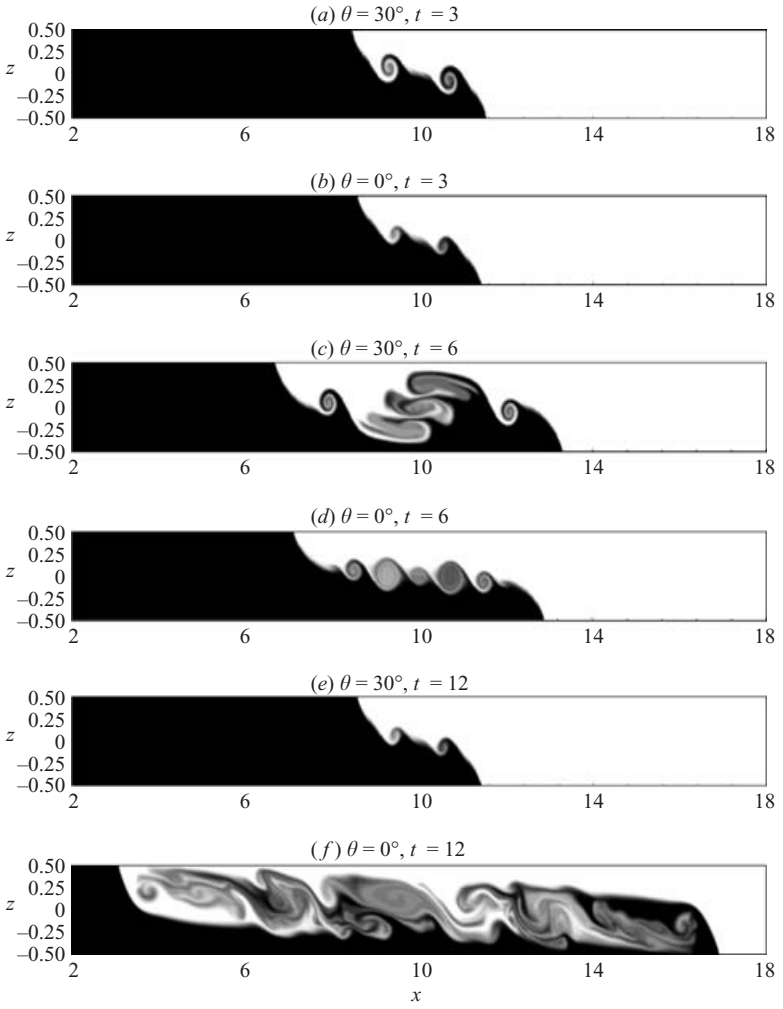


FIGURE 2. Flow evolution for $\gamma = 0.998$ and $Re = 4000$, for a horizontal channel and for a channal inclined $\theta = 30°$. Images for the two angles are shown alternately. The overturning of interfacial structures during the early stages, and the subsequent mixing during the later stages, are seen to be more intensive in the inclined channel.

increased front velocity. For both configurations the flow remains symmetrical around $(L_1, 0)$, as expected for a Boussinesq flow.

These simulation results indicate that the presence of the slope is of minor importance during the initial phase of the flow but can dominate later on. A similar observation was made by Ross, Linden & Dalziel (2002) for the release of a finite volume of fluid on a uniform slope, away from the top and side walls. By estimating the time after which the aspect ratio of the slumping-fluid volume has reached the magnitude of the gradient of the slope, these authors obtained a time scale for the influence of the slope to become important. A similar simple scaling argument allows us to estimate the time after which the effects of the slope will have reached a significant level. From investigations of lock-exchange flows over horizontal surfaces, we know that the initial acceleration results in a front velocity of the order of the buoyancy velocity, i.e. $O(\sqrt{g'H})$. For the streamwise (downslope) component of

https://doi.org/10.1017/S002211200600437X Published online by Cambridge University Press

gravity $g' \sin\theta$ to accelerate a fluid particle to the same velocity, a time

$$t_s \sim \frac{1}{\sin\theta}\sqrt{\frac{H}{g'}} \tag{4.1}$$

is required. This indicates that the effects of the slope should be comparable in magnitude with those of the slumping motion after a dimensionless time of $O(1/\sin\theta)$. A more detailed scaling argument will be developed below.

4.1.1. *Front height*

Figure 2 suggests that the height of the front in the inclined channel increases to a level that is substantially above its counterpart for a horizontal flow, as a result of two distinctly different mechanisms. Firstly, the front directly entrains ambient lighter, fluid. However, for larger angles the addition of fluid from the current behind the front becomes more important, as the average velocity of the dense fluid is substantially higher than the front velocity. In the following, we will quantify the growth of the front height. As in our earlier work (Birman *et al.* 2005), we define the height of the gravity current at the streamwise grid point x_i by integrating over the density field in the z-direction:

$$\left.\begin{aligned} h^*(x) &= \frac{1}{1-\gamma}\int_0^1 \rho(x,z)\,\mathrm{d}z - \frac{\gamma}{1-\gamma}, \\ h(x_i) &= \frac{1}{N+1}\sum_{j=-N/2}^{j=N/2} h^*(x_{i+j}). \end{aligned}\right\} \tag{4.2}$$

In Birman *et al.* (2005) it was shown that by averaging over a sliding window of N grid points, the influence of localized interfacial vortices on the height of the gravity current is reduced. We can now define the height of the front as the first maximum of $h(x_i)$ when proceeding in the negative x-direction from $x = L$. In most experiments the precise concentration distribution is unknown, so that the height as defined above cannot be obtained. Hence it is frequently determined as the highest point on the interface between the two fluids. We thus define a second measure of the local height as the highest point of the $c = 0.5$ contour:

$$\left.\begin{aligned} h_{max}(x_i) &= z' + 0.5, \\ z' &= \max_z\{\rho(x_i, z) = (1+\gamma)/2\}. \end{aligned}\right\} \tag{4.3}$$

The front height h_{max} is then defined as the first maximum of $h_{max}(x_i)$ when proceeding in the negative x-direction from $x = L$. Figure 3 shows the variation in the front height as function of time, with the data for the horizontal case shown for comparison. For the sloping case we observe an increase in both measures of the front height with time until approximately $t = 9$. The front height then attains a maximum and subsequently decreases rapidly. Beyond time $t = 12$, figure 3 shows that the front height fluctuates around a constant value close to the height for the horizontal case.

4.1.2. *Front velocity*

The front velocities $u_f(t)$ of the currents are shown in figure 4. The initial transient gives rise to an overshoot, as discussed by Härtel *et al.* (1999). Thereafter, both the sloping current and its horizontal counterpart enter an extended phase characterized by a nearly constant front velocity u_q, the speed of the front in the sloping channel being about 20 % higher. However, there is a clear difference in their long-term

https://doi.org/10.1017/S002211200600437X Published online by Cambridge University Press

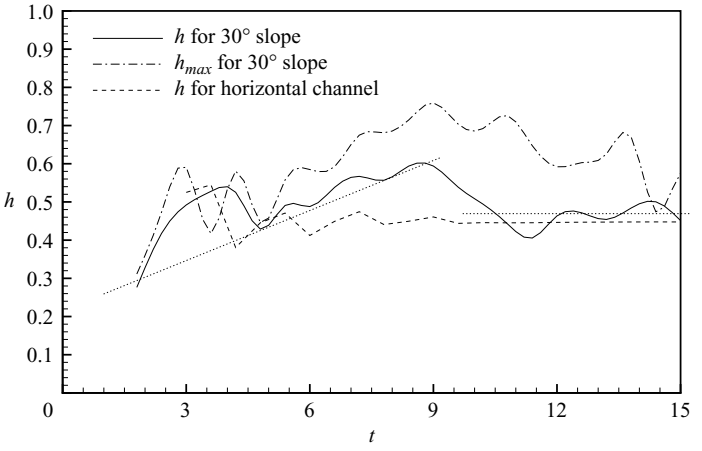


FIGURE 3. The front height as function of time for the two flows shown in figure 2. The solid and dot-dashed lines relate to the flow on the 30° slope, whereas the dashed line represents the horizontal channel. The dotted lines indicate linear fits to $h(t)$ for the early and late stages, respectively, of the flow down the 30° slope. They demonstrate a growth in the front height until approximately $t = 9$ and a nearly constant value after about $t = 12$.

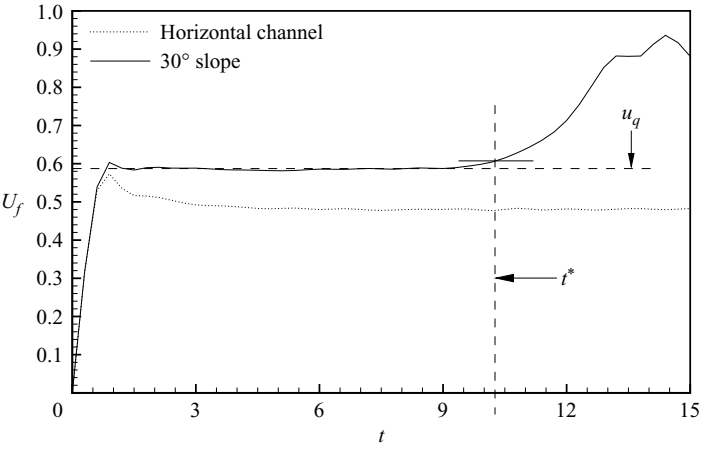


FIGURE 4. Front velocity as a function of time for the flows shown in figure 2. Solid line, 30° slope; dotted line, horizontal case. While the horizontal current maintains a constant front velocity until the end of the simulation, the sloping current undergoes a transition to a higher, unsteady, front velocity.

behaviour. While the horizontal current maintains its quasi-steady velocity u_q until the end of the simulation, the sloping current undergoes a transition, beyond time $t = 9$, when it enters a second phase characterized by an unsteady but substantially higher front velocity. During this phase, the front velocity reaches peak values that are up to 50 % higher than the quasi-steady value. We define the transition time t^* between the two phases of the sloping current as the time at which the front velocity has increased by more than 5 % above its quasi-steady velocity u_q; t^* is shown by the vertical dashed line in figure 4. We furthermore note that the decrease in height of the gravity current shown in figure 3 occurs at around the same time as the increase

https://doi.org/10.1017/S002211200600437X Published online by Cambridge University Press

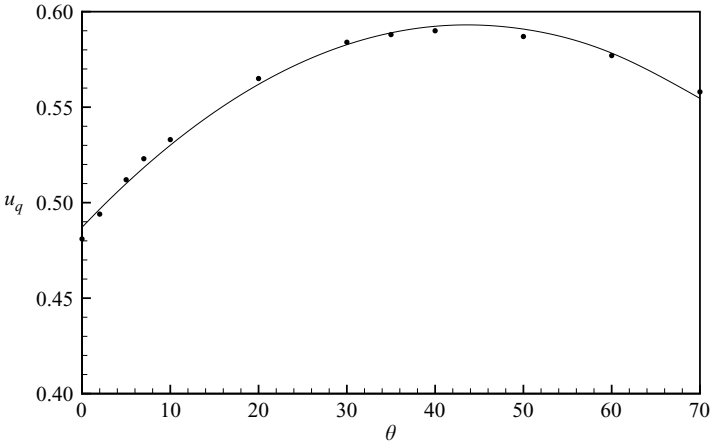


FIGURE 5. The quasi-steady front velocity u_q as a function of the slope angle θ for Boussinesq flows with $\gamma = 0.998$ and $Re = 4000$. A maximum exists around $\theta = 40^\circ$. $u_q(\theta)$ is well described by the parabolic fit $u_q = -0.1824(\theta\pi/180)^2 + 0.2781(\theta\pi/180) + 0.4871$, which is shown as a solid line.

in its front velocity. The relation between these two observations will become clearer below.

As mentioned in the introduction, the experimental study by Britter & Linden (1980) reported constant front velocities for gravity currents down uniform slopes. This does not necessarily represent a contradiction to the present findings, as the earlier investigation focused on continuously fed currents whose heights were substantially lower than the height of the tank, so that the configuration was quite different from the present lock-exchange set-up. Furthermore, the experimental data showed substantial scatter, so that an effect similar to the one observed here might not have been easily identifiable.

4.2. *Influence of the slope angle*

Figure 5 shows the dependence of the quasi-steady front velocity u_q on the angle of the slope for $Re = 4000$. A maximum of u_q is seen to exist near $\theta = 40^\circ$, with very little variation between 30° and 50°. In comparison, experiments by Zukoski (1966) for bubble motion in inclined tubes showed that a maximum velocity is reached close to 30°. A similar dependence on angle was observed for gravity currents with higher density contrasts, even though the velocities of the dense and light fronts are different in this case, as will be discussed below. Our simulations show the value of u_q to be nearly independent of Re above $Re \sim 1000$. For a discussion of the effects of the Reynolds number and the boundary conditions on the front velocity of horizontal currents, see Birman *et al.* (2005).

Figure 6 depicts the transition time t^* as a function of the slope angle θ for $Re = 4000$. The scaling law (4.1), shown as a solid line for comparison, is in reasonable agreement with the computational data. As expected, for $\theta \to 0$, $t^* \to \infty$, a transition to a higher front velocity is not observed for a gravity current in a horizontal channel. For $Re > 500$, our simulations show t^* to be nearly independent of Re. However, for $Re = 200$ no transition is observed in a simulation that was carried on until $t = 22$. Evidently at this low value of Re viscous forces are sufficiently strong to suppress the increase in the front velocity.

https://doi.org/10.1017/S002211200600437X Published online by Cambridge University Press

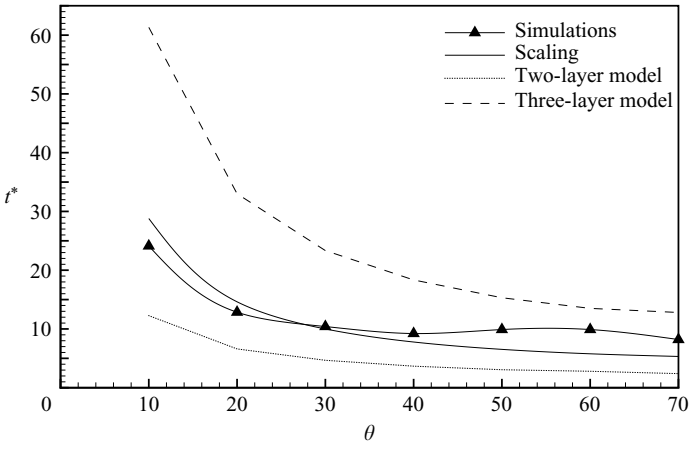


FIGURE 6. The transition time t^* at which the front velocity increases from its quasi-steady state to a higher, unsteady, value, as a function of the slope angle for Boussinesq flows with $\gamma = 0.998$ and $Re = 4000$. For comparison, the scaling law (4.1) with a suitable proportionality factor is shown. The dashed line gives the upper estimate obtained from the three-layer model discussed later in the text, while the dotted line provides the lower limit obtained from the two-layer model. The upper limit is more accurate for larger angles, while the lower limit is more accurate at smaller angles.

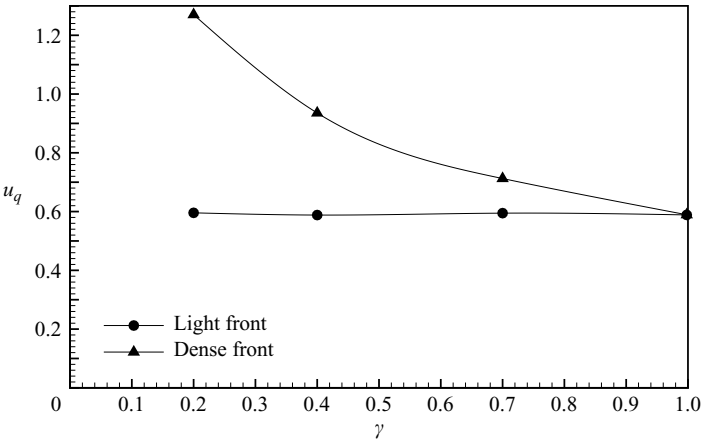


FIGURE 7. The quasi-steady dimensionless front velocities of the dense and light fronts, respectively, as functions of the density ratio γ for a slope of 30°. Similarly to the horizontal case (Birman *et al.* 2005), the velocity of the dense front (triangles) grows as the density contrast increases while the velocity of the light front (circles) does not depend on γ.

4.3. *Influence of the density ratio*

Both Lowe, Rottman & Linden (2005) and Birman *et al.* (2005) found that the dimensionless speed of the dense front increases with the density contrast, while the dimensionless speed of the light front remains essentially unchanged; see also the earlier investigations by Keller & Chyou (1991) and Gröbelbauer *et al.* (1993). The quasi-steady front velocities for non-Boussinesq flows in sloping channels show a similar trend; see figure 7. The qualitative nature of this observation is identical for all angles, although only the representative case of $\theta = 30°$ is shown here. Lowe *et al.*

https://doi.org/10.1017/S002211200600437X Published online by Cambridge University Press

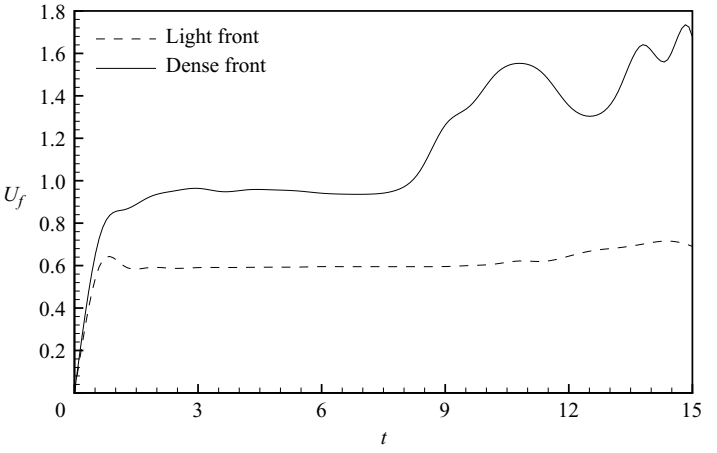


FIGURE 8. Front velocities vs. time for $\gamma = 0.4$, $\theta = 40^\circ$ and $Re = 4000$. Solid line, dense front; dashed line, light front. The transition occurs earlier, and is more pronounced, for the dense front.

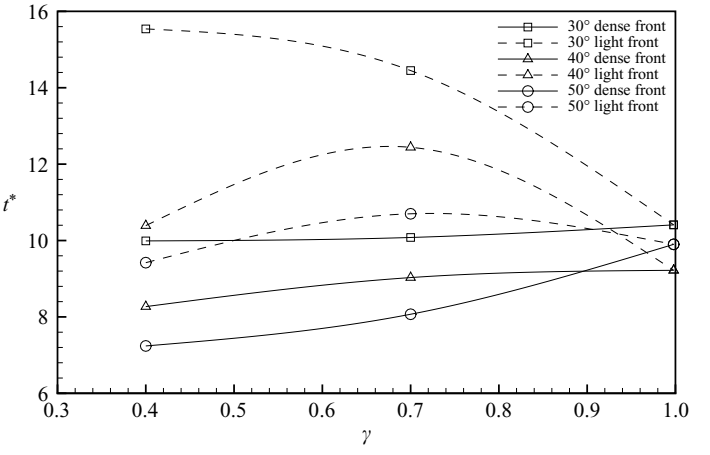


FIGURE 9. Transition times for dense (dashed lines) and light (solid lines) fronts at angles $\theta = 30^\circ$ (squares), 40° (triangles) and 50° (circles), as functions of the density ratio. For all density ratios and angles, the transition occurs earlier for the dense front.

(2005) and Birman *et al.* (2005) furthermore observed that the height of the light front remains unchanged, while that of the dense front decreases with increasing density contrast. Here we find that these observations remain valid for flows on slopes.

Figure 8 shows the front velocity for a non-Boussinesq flow with $\gamma = 0.4$ on a slope $\theta = 40^\circ$. We observe that the transition from the quasi-steady velocity to a higher, unsteady, velocity is quite pronounced for the heavy front, whereas for the light front the increase is hardly noticeable and occurs at a later time. Results from corresponding simulations for a variety of density ratios are summarized in figure 9, which depicts the transition time t^* as function of the density ratio for both fronts.

4.4. *Mixing*

Figure 2 demonstrated a profound influence of the slope angle on the vortical structures along the interface. In particular, large-scale interfacial turnover events

https://doi.org/10.1017/S002211200600437X Published online by Cambridge University Press

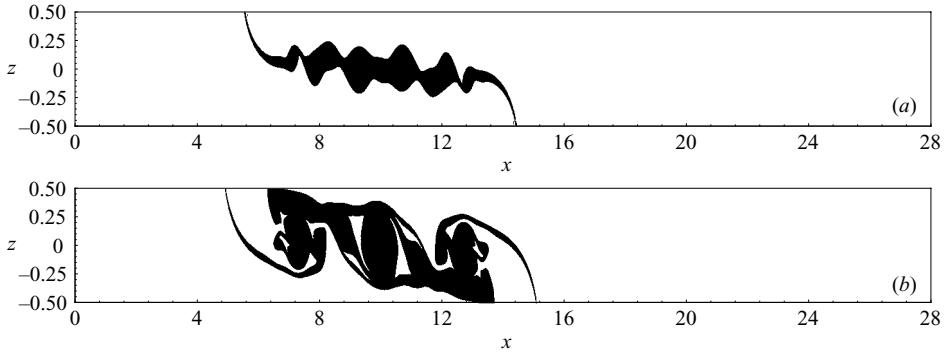


FIGURE 10. The mixing behaviour of the flows shown in figure 2: the mixed regions (shown in black), as defined by (4.4) at time $t = 9$, for (a) the horizontal and (b) the $\theta = 30^\circ$ configurations. The mixed region is observed to grow much more rapidly for the sloping lock-exchange flow.

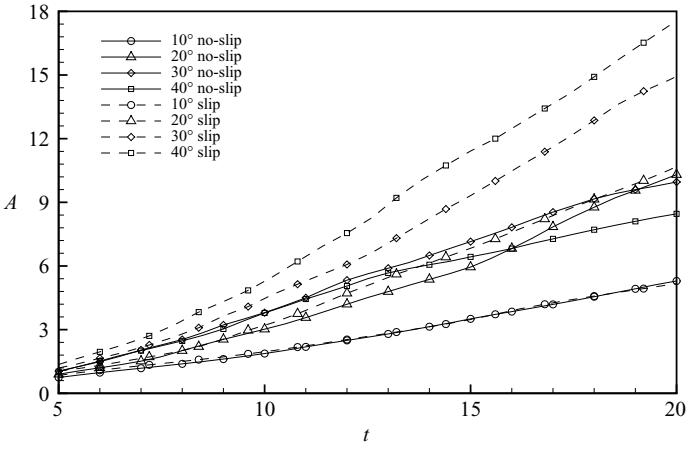


FIGURE 11. The size of the mixed region as a function of time for slope angles of 10° (circles), 20° (triangles), 30° (diamonds) and 40° (squares). Both no-slip (solid lines) and slip (dashed lines) boundaries are considered. $Re = 4000$ and $\gamma = 0.998$.

were observed in the tilted configuration, whereas such events were absent in the horizontal geometry. The corresponding plots of the concentration field suggest that the mixing of the fluids is increased by these large-scale turnover events. In order to quantify these observations, we define the mixed region to be the region whose density is such that

$$\rho_2 + \tfrac{1}{10}\Delta\rho < \rho < \rho_1 - \tfrac{1}{10}\Delta\rho, \tag{4.4}$$

where $\Delta\rho = \rho_1 - \rho_2$. Figure 10 provides an example of the size of the mixed region at identical times for the horizontal and tilted geometries, showing that the mixed region in the tilted configuration is substantially larger. Figure 11 summarizes the simulation results for the size A of the mixed region as a function of time for slope angles between 0° and 40°, for both no-slip and slip conditions at the top and bottom walls. For slip boundaries, mixing increases uniformly with the angle, for the range of angles considered here. This reflects the fact that for slip walls most of the mixing is due to the Kelvin–Helmholtz instability and subsequent large-scale eddy turnover events at the interface, which are enhanced at larger angles. For no-slip walls, the

https://doi.org/10.1017/S002211200600437X Published online by Cambridge University Press

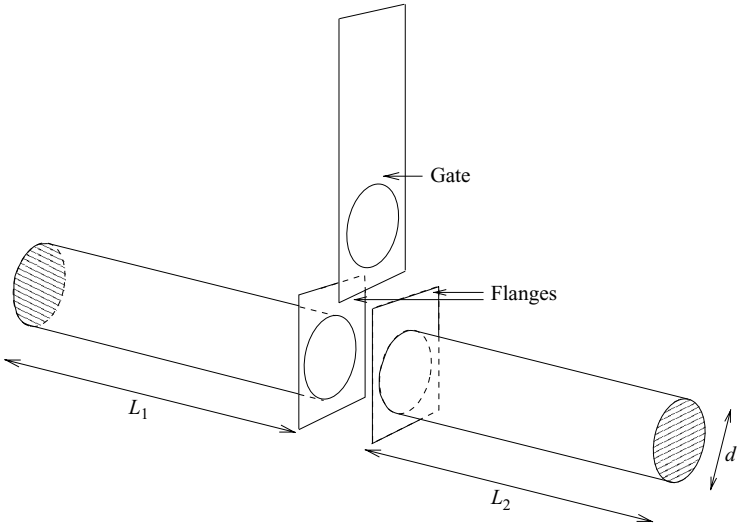


FIGURE 12. The experimental set-up employs two circular tube segments of diameter d. One end of each segment can be closed with a rubber stopper, while the opposite ends have flanges that can be attached to each other. A sliding gate is inserted in between the flanges. The gate consists of a thin rectangular plate from which a circular cross-section of diameter d has been cut out. The tube segments are filled with fresh and salt water, respectively, with the gate in the closed position. The flow starts when the gate is opened, by sliding it to a position such that the circular cutout aligns with the tube segments.

mixing during the early stages of the flow is enhanced on increasing the slope from $\theta = 10^\circ$ to $\theta = 30^\circ$. Beyond the latter angle, no significant improvement in mixing is observed as the steepness of the slope is further increased. In fact, during the late stages the flow for $\theta = 40^\circ$ is less well mixed than for 20° or 30°.

5. Experiments

In order to validate the above simulation results, and to verify the existence of two separate phases characterized by different front velocities, we conducted a set of conceptually straightforward experiments for a range of slopes. These were carried out in a cylindrical Plexiglas tube inclined at angles varying from $\theta = 0^\circ$ to 30°. The length of the tube was 180 cm, while it had a diameter of 2.3 cm. A cylindrical tube, rather than a rectangular channel, was employed in order to minimize the influence of the side walls and any three-dimensional front dynamics triggered or enhanced by them. The tube was fitted with a sliding gate in the middle (figure 12), which was removed at the start of the experiment. To keep the experiments simple, a density ratio $\gamma = 0.988$ was used each time; this was well within the Boussinesq regime. As a result of the different geometries, the comparison with the simulations can clearly be only qualitative. However, for demonstrating the existence of two distinct phases this was deemed sufficient.

The experiments were conducted inside a large tank filled with fresh water, in order to reduce reflections from the tube's surface. After being positioned at the desired angle, the lower half of the tube was filled with fresh water. The sliding gate was then closed, and denser salt water was used to fill the upper half of the tube. Red food colouring was added to the salt water in order to aid visualization. The density of the salt water in all the experiments was $1.010\,\mathrm{g\,cm^{-3}}$ while the density of fresh water

https://doi.org/10.1017/S002211200600437X Published online by Cambridge University Press

was $0.998\,\mathrm{g\,cm^{-3}}$, giving $\gamma = 0.988$. The gravity current was released by opening the sliding gate. All experiments were recorded by digital camera. These recordings were subsequently analysed to determine the front position and speed as functions of time, by measuring the time required for the front to travel fixed-length intervals marked on the tube.

5.1. *Experimental results*

Figure 13 displays flow-visualization images of the experiment with a slope of 20°. Only the half of the tube originally containing fresh water is shown; the dense-salt-water current appears darker than the surrounding fresh water. Interfacial billows due to the presence of shear instability can be recognized. As t increases, both the height and the steepness of the dense front are seen to increase, in a fashion that resembles the computational images shown in figure 2.

Figure 14 depicts the front velocity as function of time for a slope of 20°. During the initial phase, until about $t = 9$, the front velocity is seen to have a fairly constant value. It subsequently transitions to a higher value and finally exhibits unsteady fluctuations that are similar to, but somewhat smaller than, those observed in the numerical simulations. We assume that these differences are due to the different geometries. This experimental observation confirms the numerical findings regarding the existence of distinct phases. The values of the transition times t^* (12.6 in the simulation and between 11 and 12 in the experiment) compare favourably, which is perhaps surprising, considering the different geometries.

Figure 15 displays the dependence of the quasi-steady front velocity on the slope angle. Results from the circular tube experiments of Séon *et al.* (2005) are shown for comparison, along with an experimental data point from figure 12.2 of Simpson (1997) for a horizontal tube. While the overall agreement is satisfactory, the velocity values measured in the present study are somewhat higher than the comparison data for non-zero angles. One reason for this discrepancy may be the difference in the values of the Reynolds number: in our experiments Re was close to 1250 while in the experiments of Séon *et al.* (2005) Re was less than 1000. No value of Re was provided for the horizontal-tube experiment of Simpson (1997). While the experiments by Séon *et al.* (2005) covered a wide range of angles, those authors only analysed the values of the quasi-steady front velocities, without commenting on the existence of different phases.

6. Simplified flow models

The above numerical-simulation results and corresponding experimental observations suggest that during the early phase the front velocity of the gravity current is governed by the local dynamics in the region near the front but that a different mechanism takes over at a later time. In order to identify this mechanism, it is helpful to realize that the growing central region of the flow field – the region connecting the two fronts – is characterized by two layers travelling in opposite directions. If the tank is tilted with respect to the horizontal, these layers are subject to gravitational acceleration, as shown by Thorpe (1968). It is reasonable to expect that as this region grows it will eventually dominate the dynamics of the entire flow field and overwhelm the local mechanisms that are active in the neighbourhood of each front. On the basis of the analysis of Thorpe (1968), we will now describe a conceptually simple model that captures the dynamics in this central region of the flow field, in order to develop a quantitative estimate of the transition time between

https://doi.org/10.1017/S002211200600437X Published online by Cambridge University Press

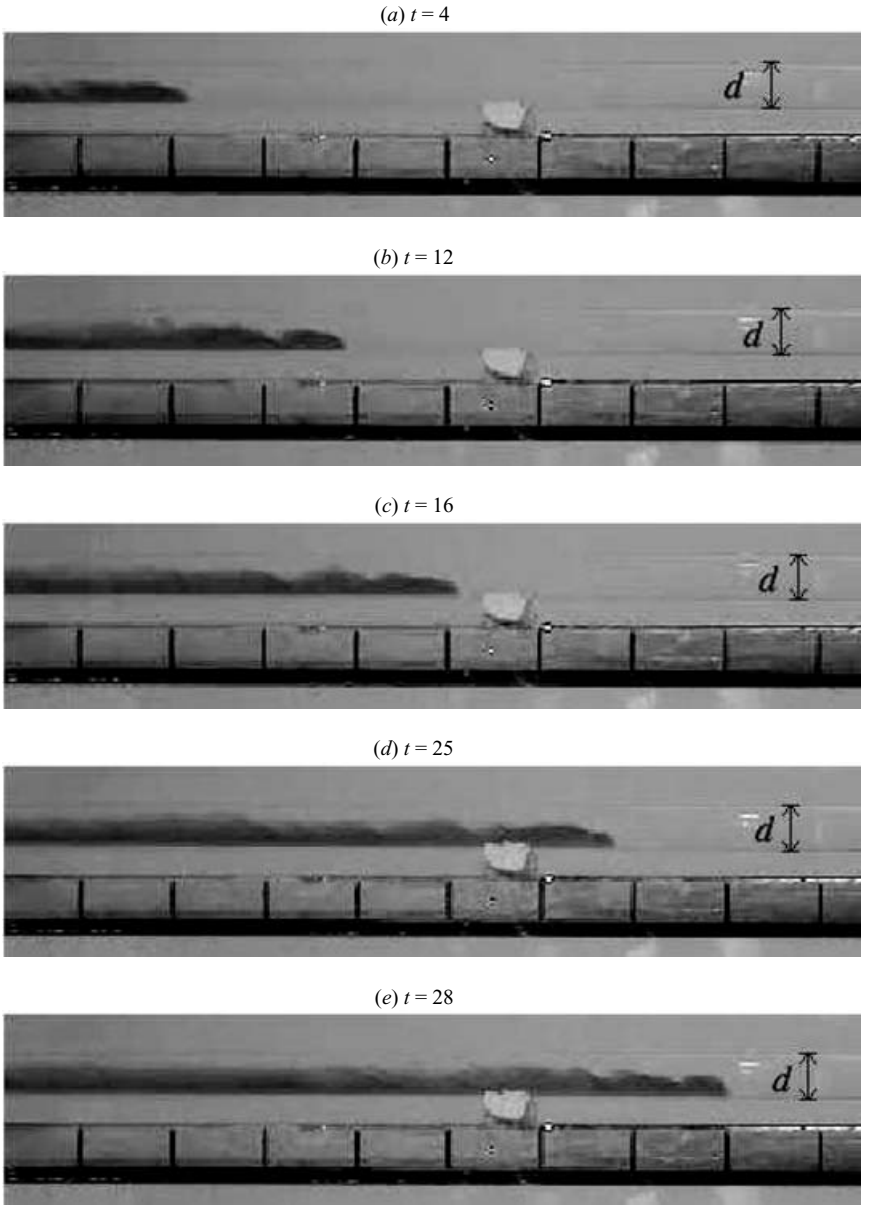


FIGURE 13. Experimental flow-visualization images for $\theta = 20°$, $\gamma = 0.988$ and $Re = 1250$ at different times. The dense-salt-water front (dark colour) moves from left to right. The gate at the centre of the tube is located just beyond the left-hand edge of the image. The diameter of the tube is d. The distance between the solid lines is 5 cm (≈ 2.174 tube diameters).

the early and late phases of the flow. We will then compare the estimate provided by the model with the results obtained from the numerical simulations.

6.1. *Layered flow in a sloping channel*

Consider the layered unidirectional motion of a stratified fluid between two parallel plates, located at $z = 0$ and H, inclined at an angle θ to the horizontal. The effects of viscosity and diffusion are ignored, as are the side- or endwalls. The coordinate

https://doi.org/10.1017/S002211200600437X Published online by Cambridge University Press

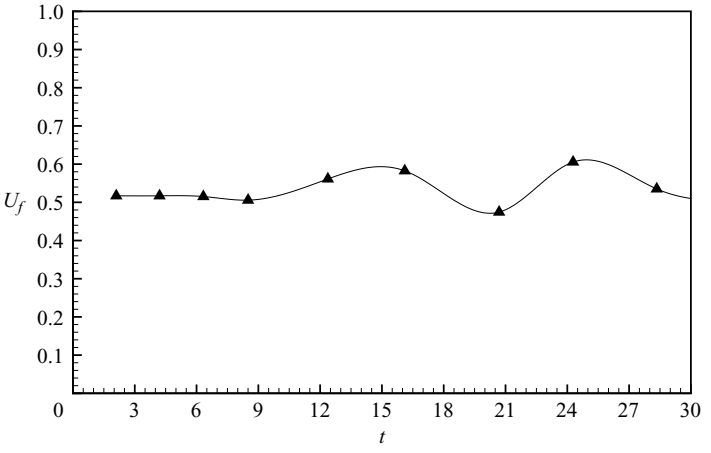


FIGURE 14. Experimental front velocity as function of time for $\theta = 20°$, $\gamma = 0.988$ and $Re = 1250$. Quasi-Steady front propagation is observed until about $t = 9$. Subsequently, a transition occurs to a second phase which is characterized by a larger, unsteady, front velocity.

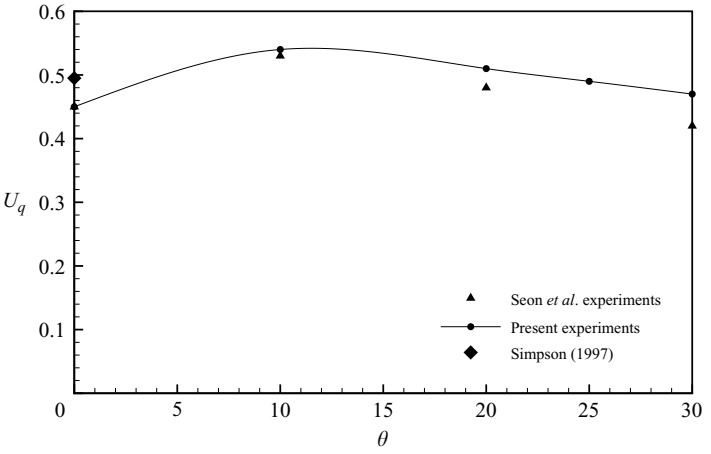


FIGURE 15. The quasi-steady front velocity as a function of the slope angle. The circles represent the present, two-dimensional, data. The triangles denote experimental results for inclined tubes from Séon *et al.* (2005), while the data point marked with a diamond symbol was taken from Simpson (1997).

system is defined as in figure 1. The density depends on z only, $\rho = \rho(z)$, whereas the velocity in the x-direction depends on both z and time, $u = u(z, t)$. The equations of motion are

$$\rho \frac{\partial u}{\partial t} = -\frac{\partial p}{\partial x} + g\rho \sin\theta, \tag{6.1}$$

$$0 = -\frac{\partial p}{\partial z} - g\rho \cos\theta. \tag{6.2}$$

Note that the above equations hold for arbitrary density profiles, i.e. they are not limited to the Boussinesq regime. Thorpe (1968) provided a solution to these equations,

https://doi.org/10.1017/S002211200600437X Published online by Cambridge University Press

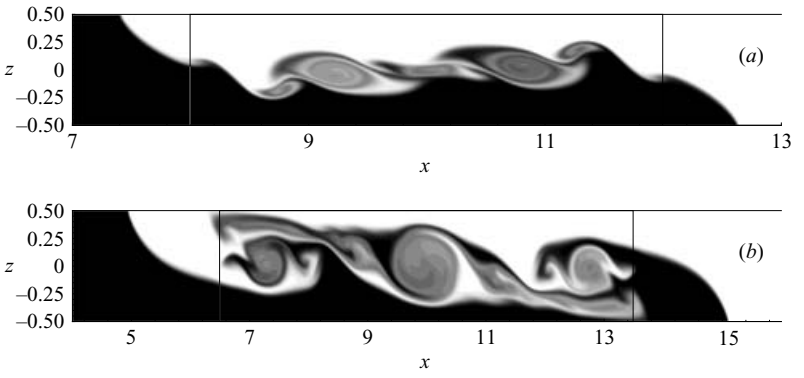


FIGURE 16. Typical concentration fields during (*a*) the early ($t = 4.8$) and (*b*) the late ($t = 9$) phases of a gravity current for $\theta = 30°$, $\gamma = 0.998$ and $Re = 4000$. The solid vertical lines show the region of integration for obtaining the layer-averaged density profile $\rho(z)$.

which for our dimensionless variables reads

$$u(z,t) = \frac{t\sin\theta}{1-\gamma}\left(1 - \frac{1}{\rho(z)\displaystyle\int_{-0.5}^{0.5}\rho^{-1}\,\mathrm{d}z}\right). \tag{6.3}$$

This relationship allows us to compute $u(z,t)$ for any given density profile $\rho(z)$. The numerical-simulation results provide some guidance as to the qualitative and quantitative nature of the density stratification in the central part of the flow field, so that we can employ them to obtain an estimate for $\rho(z)$. As we will see below, during the early stages of the flow the overall density field is approximated closely by a two-layer model, whereas a three-layer model is more appropriate later on. Hence we will discuss both of these models in the following, as limiting cases.

6.1.1. *Two-layer model*

Figure 16(*a*) shows a typical density field from the early stages of the simulation. By integrating this density field in the x-direction between the two x-locations indicated in the figure, we obtain the streamwise-averaged density profile $\rho(z)$ represented in figure 17(*a*) by the dashed line. This profile can be approximated reasonably closely by a two-layer model, as indicated by the solid line shown in the same figure. This profile is given by

$$\rho(z) = \begin{cases} 1, & -0.5 \leqslant z \leqslant 0, \\ \gamma, & 0 < z \leqslant 0.5. \end{cases} \tag{6.4}$$

In conjunction with (6.3) this yields the following velocities for the two-layer system:

$$u_{2l}(z) = \begin{cases} \dfrac{t\sin\theta}{1+\gamma}, & -0.5 \leqslant z \leqslant 0, \\ \dfrac{-t\sin\theta}{1+\gamma}, & 0 < z \leqslant 0.5. \end{cases} \tag{6.5}$$

https://doi.org/10.1017/S002211200600437X Published online by Cambridge University Press

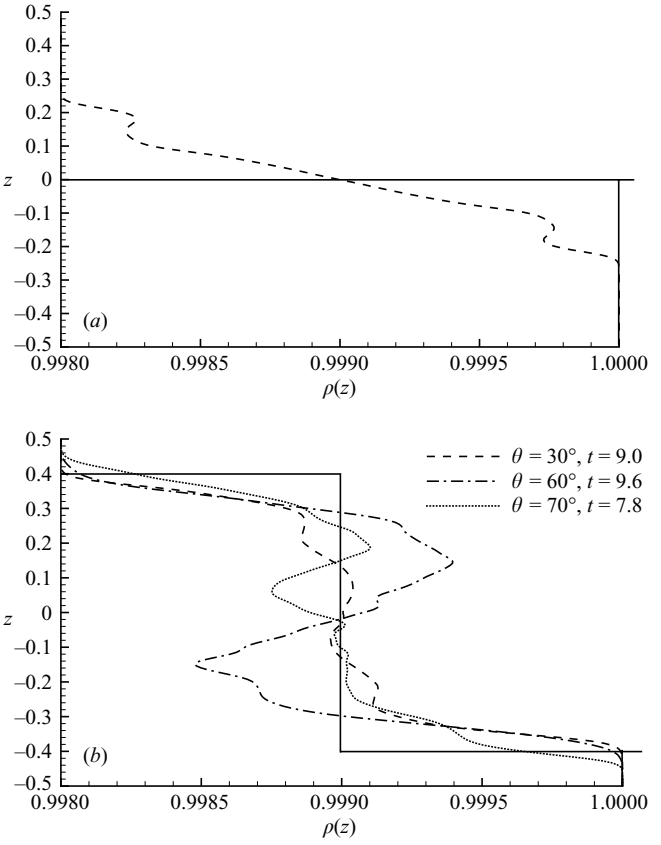


FIGURE 17. Layer-averaged density stratification profiles for the flow shown in figure 16. Dashed lines, density profiles obtained by integrating the simulation data; solid lines, approximation of the integrated simulation data by (*a*) a two-layer model for $\theta = 30^\circ$ and $t = 4.8$, and (*b*) a three-layer model.

Thus the average acceleration of the fluid layer between $z = -0.5$ and $z = 0$ is given by

$$\overline{a}_{2l} = \frac{\sin\theta}{1+\gamma}. \tag{6.6}$$

6.1.2. *Three-layer model*

During the later stages of the flow, the fluids have become much more thoroughly mixed across the central core section of the channel. A typical simulation result is shown in figure 16(*b*). By integrating along the x-axis in the interval indicated, we obtain the profile shown by the dashed line in figure 17(*b*). For a wide range of angles, we observe a well-mixed region in the centre of the channel, embedded between regions of nearly pure fluid close to the walls. The evolution of this mixed-fluid layer in the central region of the channel has also been studied experimentally by Thorpe (1971) and Staquet (2000). In the experiments carried out by Thorpe (1971), the layers were initially accelerated by tilting the channel. Subsequently, the channel was brought back to its horizontal position. Thorpe observed that the thickness of the mixed layer initially increased and subsequently approached a constant value of about 60 % of the channel depth for the horizontal configuration. In the present case

https://doi.org/10.1017/S002211200600437X Published online by Cambridge University Press

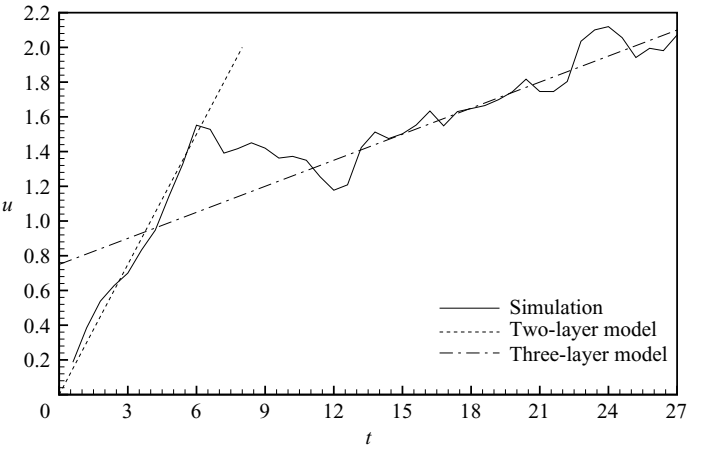


FIGURE 18. The average velocity of the fluid layer $-0.5 \leqslant z \leqslant 0$ at the gate location, as a function of time. Solid line, simulation data; dashed line, two-layer model, dot-dashed line: three-layer model. The two- and three-layer models are seen to yield good agreement with the simulation data during the early and late stages of the flow, respectively.

of an inclined channel, we observe that the mixed layer occupies nearly 80 % of the channel depth for a wide range of angles, as can be seen in figure 17(*b*). Hence we approximate the resulting stratification for Boussinesq flows as

$$\rho(z) = \begin{cases} 1, & -0.5 \leqslant z \leqslant -0.5 + h, \\ \dfrac{1+\gamma}{2}, & -0.5 + h < z \leqslant 0.5 - h, \\ \gamma, & 0.5 - h < z \leqslant 0.5, \end{cases} \tag{6.7}$$

where the value $h = 0.1$ is suggested by figure 17(*b*). Together with (6.3) this gives for the velocities in the three-layer system

$$u_{3l}(z) = \begin{cases} \dfrac{1+9\gamma}{\gamma^2+18\gamma+1} t \sin\theta, & -0.5 \leqslant z \leqslant -0.4, \\ \dfrac{(1-\gamma)}{\gamma^2+18\gamma+1} t \sin\theta, & -0.4 < z \leqslant 0.4, \\ -\dfrac{9+\gamma}{\gamma^2+18\gamma+1} t \sin\theta, & 0.4 < z \leqslant 0.5. \end{cases} \tag{6.8}$$

For the average acceleration of the fluid layer in the interval $-0.5 < z < 0$ we thus obtain

$$\bar{a}_{3l} = \frac{(1+\gamma)\sin\theta}{\gamma^2+18\gamma+1}.$$

6.2. *Comparison with the simulations*

For the flow shown in figure 16, the vertically averaged velocity of the dense layer at the gate location is presented in figure 18. The solid line indicates the time-dependent numerical simulation result, while the slopes of the straight lines represent the acceleration values provided by the model. Here the dashed line corresponds to the two-layer model while the dash-dotted line is obtained from the three-layer model. Good agreement between the simulation data and the model predictions is observed.

https://doi.org/10.1017/S002211200600437X Published online by Cambridge University Press

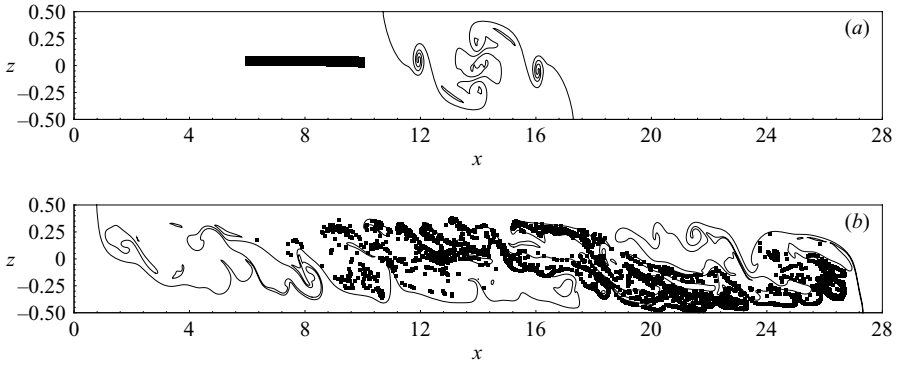


FIGURE 19. Passive tracer particles, represented by black dots, in the flow shown in figure 2, but with $L_1 = 14$, at times (*a*) 8 and (*b*) 20. The shape of the current is indicated by the solid line, which marks the density contour $\rho = 0.5(1 + \gamma)$. Even though the marker particles are initially placed far behind the front, they eventually catch up with it, demonstrating the addition of dense fluid to the current head from behind.

The two-layer model provides an accurate description of the average acceleration of the fluid in the lower half of the channel during the early phase, while the three-layer model is more appropriate for the later stages. The transition between these two phase is seen to occur during the time interval $6 < t < 12$, which is in good agreement with the value $t^* \approx 10$ determined earlier; see figure 6.

Figure 18 indicates that the fluid layers in the upper and lower halves of the channel are continuously accelerating while the current fronts move with constant velocity during the early, quasi-steady, phase, as shown in figure 5. (It is interesting to note that Britter & Linden (1980) made similar observations for a flow that is qualitatively different, i.e. a deeply submerged continuous current.) Hence the head has to absorb additional dense fluid from behind, which results in its growth, as confirmed numerically in figure 3. This growth of the current front cannot be sustained forever, so that after a certain time the front itself will have to accelerate in response to the faster fluid coming from behind. These observations suggest that the transition from a lower, constant, front velocity to a higher, unsteady, velocity will occur when a sufficient amount of dense fluid has caught up with the front. This process of catching-up can be observed in the simulations by tracking passive marker particles initially placed in the dense fluid far behind the front; see figure 19. Over time, these particles accelerate towards the front and eventually catch up with it.

We now provide an upper and lower estimate for the transition time. We assume that the transition occurs when the streamwise (downslope) component of the gravity vector has had sufficient time to accelerate fluid initially at rest near the gate location, so that this fluid now catches up with the steadily moving front. If mixing is negligible during this catch-up phase, the two-layer model will yield an appropriate estimate of the transition time. This estimate represents a lower limit, since some mixing will always reduce the fluid acceleration and increase the transition time. If, however, we assume the three-layer model from the very start, we obtain an upper estimate of the transition time, since we incorporate some aspects of mixing even during the initial stages of the flow, when there is very little of it. Note that the three-layer model incorporates the effects of mixing on the density profile, while it does not account for the cross-stream transfer of momentum due to convective mixing. As upper and

https://doi.org/10.1017/S002211200600437X Published online by Cambridge University Press

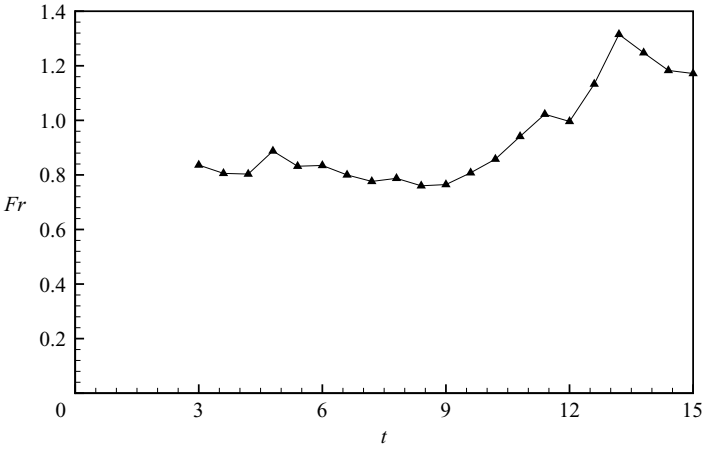


FIGURE 20. The Froude-number Fr as a function of time for the gravity current down a slope shown in figure 2. Fr decreases somewhat from $t = 5$ until $t = 9$, as the front height increases, while the front velocity remains constant. Thereafter, the front velocity transitions to a higher value while the front height decreases, resulting in an increase in Fr.

lower estimates for the transition time we thus obtain

$$t_u^* = 2u_q/\overline{a}_{3l}, \tag{6.9}$$

$$t_l^* = 2u_q/\overline{a}_{2l}. \tag{6.10}$$

Figure 6 shows the upper and lower estimates thus obtained for comparison with the simulation data for t^*. The upper estimate is seen to represent a better approximation of t^* at larger angles, where mixing is more intense, while the lower bound is more accurate for smaller angles, where mixing is limited.

7. Summary and conclusions

High-resolution simulations based on the Navier–Stokes equations have shown that sloping lock-exchange flows go through an initial quasi-steady phase that is characterized by a constant front velocity. This quasi-steady front velocity has a maximum for slope angles around 40°, and it persists up to a dimensionless time of the order of 10. The flow subsequently undergoes a transition to a second phase during which the front velocity shows unsteady fluctuations but is generally larger than the quasi-steady value. These computational findings are confirmed by experimental observations of lock-exchange flows in a tube having a circular cross-section.

The reason for the observed transition from a quasi-steady front velocity to a larger unsteady, value is found in the continuous acceleration of the stratified fluid layers connecting the two fronts, by the streamwise (downslope) component of the gravity vector. This acceleration leads to a situation where the fluid layers behind the current front move faster than the front itself. Similar features were also observed by Britter & Linden (1980) for the qualitatively different situation of deeply submerged continuous currents. For the flow shown in figure 2, we saw in figure 3 that the head height increases between $t = 5$ and $t = 9$, while according to figure 4 the front velocity remains unchanged. Hence, as shown in figure 20 that, the Froude number Fr decreases slightly during this phase. Here, Fr is formed from the front velocity u_f,

https://doi.org/10.1017/S002211200600437X Published online by Cambridge University Press

the reduced gravity g of and the front height h of the current:

$$Fr = \frac{u_f}{\sqrt{gh}}. \tag{7.1}$$

Eventually, the current front is unable to absorb more fluid from behind and its velocity has to increase, thereby triggering the transition to the second, unsteady, phase. During this transition, the front height decreases as the front velocity increases, which results in a growth of Fr by about 50 %. The transition time was determined as function of the slope and the density ratio of the two fluids. A series of simulations that does not invoke the Boussinesq approximation demonstrates that for increasing density contrast the transition occurs earlier for the denser current.

A pair of conceptually simple models, based on the analysis of Thorpe (1968), with different density profiles was employed for the flow in the region connecting the fronts. The simulation results show that for the early stages of the flow a two-layer stratification model is appropriate, while the later stages require a three-layer stratification model, owing to the intense mixing in the central part of the channel cross-section. These models are employed to estimate the time after which the accelerating stratified fluid layers will affect the velocities of the current fronts. In this way, the models are shown to provide upper and lower estimates for the transition time, in good agreement with the simulation results.

It remains to be seen if and how the above observations will be affected by the possibility of spanwise variations in a three-dimensional flow. Efforts in this direction are currently under way.

The authors wish to acknowledge very fruitful discussions with Professors Tony Maxworthy and Jim Rottman. This work was supported by NSF through grant CTS-0209194, as well as through an equipment grant. Additional funding was provided by BHP Billiton Petroleum and by ExxonMobil. The experiments were carried out by VKB during a visit to UCSD. The hospitality of the research group around Paul Linden and Jim Rottman is gratefully acknowledged.

REFERENCES

Beghin, P., Hopfinger, E. J. & Britter, R. E 1981 Gravitational convection from instantaneous sources on inclined boundaries. *J. Fluid Mech.* **107**, 407.

Benjamin, T. B. 1968 Gravity currents and related phenomena. *J. Fluid Mech.* **31**, 209.

Birman, V. K., Martin, J. E. & Meiburg, E. 2005 The non-Boussinesq lock-exchange problem. Part 2. High resolution simulations. *J. Fluid Mech.* **537**, 125.

Bonnecaze, R., Huppert, H. E. & Lister, J. R. 1993 Particle-driven gravity currents. *J. Fluid Mech.* **250**, 339.

Bonnecaze, R. & Lister, J. 1999 Particle-driven gravity currents down planar slopes. *J. Fluid Mech.* **390**, 75.

Britter, R. & Linden, P. 1980 The motion of the front of a gravity current travelling down an incline. *J. Fluid Mech.* **99**, 531.

Britter, R. & Simpson, J. E. 1978 Experiments on the dynamics of a gravity current head. *J. Fluid Mech.* **88**, 223.

Cantero, M. I., Lee, J. R., Balachandar, S., Garcia, M. H. & Ha, M. Y. 2006 On the front velocity of gravity currents. *J. Fluid Mech.* (submitted).

Ellison, T. & Turner, J. 1959 Turbulent entrainment in stratified flow. *J. Fluid Mech.* **6**, 423.

Etienne, J., Hopfinger, E. J. & Saramito, P. 2005 Numerical simulations of high density lock-exchange flows. *Phys. Fluids* **17**, 036601.

Gröbelbauer, H. P., Fanneløp, T. K. & Britter, R. E. 1993 The propagation of intrusion fronts of high density ratio. *J. Fluid Mech.* **250**, 669.

https://doi.org/10.1017/S002211200600437X Published online by Cambridge University Press

Hacker, J., Linden, P. F. & Dalziel, S. B. 1995 Mixing in lock-release gravity currents. *Dyn. Atmos. Oceans* **24**, 183.

Hallworth, M., Huppert, H., Phillips, J. & Sparks, S. 1996 Entrainment into two-dimensional and axisymmetric turbulent gravity currents. *J. Fluid Mech.* **308**, 289.

Hallworth, M. A., Phillips, J. C., Huppert, H. E. & Sparks, S. J. 1993 Entrainment in turbulent gravity currents. *Nature* **362**, 829.

Härtel, C., Meiburg, E. & Necker, F. 1999 Vorticity dynamics during the start-up phase of gravity currents. *Il Nuovo Cimento C* **22**, 823.

Härtel, C., Meiburg, E. & Necker, F. 2000 Analysis and direct numerical simulation of the flow at a gravity-current head. part 1. flow topology and front speed for slip and no-slip boundaries. *J. Fluid Mech.* **418**, 189.

Huppert, H. E. & Simpson, J. 1980 The slumping of gravity currents. *J. Fluid Mech.* **99**, 785.

Joseph, D. & Renardy, Y. 1992 *Fundamentals of Two-Fluid Dynamics, Part II*. Springer.

Keller, J. J. & Chyou, Y. P. 1991 On the hydraulic lock-exchange problem. *Z. Angew. Math. Phys.* **42**, 874.

Lele, S. K. 1992 Compact finite difference schemes with spectral-like resolution. *J. Comput. Phys.* **103**, 16.

Lowe, R. J., Rottman, J. W. & Linden, P. F. 2005 The non-Boussinesq lock exchange problem. part 1. theory and experiments. *J. Fluid Mech.* **537**, 101.

Maxworthy, T. & Nokes, R. 2006 Experiments on gravity currents propagating down slopes in open channels. Part 1. The effect of initial conditions on the release of a fixed volume of heavy fluid from an enclosed lock. *J. Fluid Mech.* (submitted).

Necker, F., Härtel, C., Kleiser, L. & Meiburg, E. 2002 High-resolution simulations of particle-driven gravity currents. *Intl J. Multiphase Flow* **28**, 279–300.

Necker, F., Härtel, C., Kleiser, L. & Meiburg, E. 2005 Mixing and dissipation in particle-driven gravity currents. *J. Fluid Mech.* **545**, 339.

Ross, A. N., Linden, P. F. & Dalziel, S. B. 2002 Three-dimensional gravity currents on slopes. *J. Fluid Mech.* **453**, 239.

Rottman, J. W. & Simpson, J. E. 1983 Gravity currents produced by instantaneous releases of a heavy fluid in a rectangular channel. *J. Fluid Mech.* **135**, 95.

Séon, T., Hulin, J. P. & Salin, D. 2005 Buoyancy driven miscible front dynamics in tilted tubes. *Phys. Fluids* **17**, 031702.

Shin, J. O., Dalziel, S. B. & Linden, P. F. 2004 Gravity currents produced by lock exchange. *J. Fluid Mech.* **521**, 1.

Simpson, J. E. 1997 *Gravity Currents in the Environment and the Laboratory*. Cambridge University Press.

Simpson, J. E. & Britter, R. E. 1979 The dynamics of the head of a gravity current advancing over a horizontal surface. *J. Fluid Mech.* **94**, 477.

Staquet, C. 2000 Mixing in a stably stratified shear layer: two- and three-dimensional numerical experiments. *Fluid Dyn. Res.* **27**, 367–404.

Thorpe, S. A. 1968 A method of producing a shear flow in a stratified fluid. *J. Fluid Mech.* **32**, 693.

Thorpe, S. A. 1971 Experiments on the instability of stratified shear flows: miscible fluids. *J. Fluid Mech.* **46**, 299–319.

Tickle, G. 1996 A model of the motion and dilution of a heavy gas cloud released on a uniform slope in calm conditions. *J. Haz. Mat.* **49**, 29.

Webber, D., Jones, S. & Martin, D. 1993 A model of motion of a heavy gas cloud released on a uniform slope. *J. Haz. Mat.* **33**, 101.

Zukoski, E. E. 1966 Influence of viscosity, surface tension and inclination angle on motion of long bubbles in closed tubes. *J. Fluid Mech.* **25**, 821.

https://doi.org/10.1017/S002211200600437X Published online by Cambridge University Press